RSC Advances

PAPER

View Article Online
View Journal | View Issue

Check for updates

Cite this: *RSC Adv.*, 2017, **7**, 23994

# A comprehensive understanding of water photooxidation on $Ag_3PO_4$ surfaces†

Zuju Ma,[a] Sen Lin,[b] Rongjian Sa,[a] Qiaohong Li[a] and Kechen Wu*[a]

The oxygen evolution reaction (OER) is known to be the bottleneck of water-splitting. $Ag_3PO_4$ is a highly efficient visible light photocatalyst for dye degradation and water oxidation to $O_2$, with a higher OER rate than $BiVO_4$ and $WO_3$. Despite extensive studies on $Ag_3PO_4$, the surface properties including surface electronic states, reaction sites and mechanisms of OER on $Ag_3PO_4$ surfaces are not clear at present. Herein, we reported a comparative first-principles density functional theory study of the bulk, surface properties and the mechanism of OER on the three primary low index facets of $Ag_3PO_4$: (100), (110) and (111). We revealed for the first time that the rate-limiting step of the OER on $Ag_3PO_4$ (100), (110) and (111) surfaces is the dehydrogenation of HO* (HO* → O* + $H^+$ + $e^-$), which is different from most reported metal oxides and nitrides like $TiO_2$ and g-$C_3N_4$. The OER process on the (100) surface tends to proceed by following a different mechanism as that on the (110) and (111) surfaces. The illumination of the $Ag_3PO_4$ (100), (110), and (111) surfaces with solar light provides enough overpotential for the OER to proceed spontaneously. In particular, the free energy change of removal of the first proton from water on the $Ag_3PO_4$ (111) surface is much lower than that on (100) and (110) surfaces, giving an explanation for the experimentally observed higher catalytic activity of the (111) surface. The exposed phosphorus atoms on the $Ag_3PO_4$ (111) surface promote the dehydrogenation of $H_2O$ and suppress the formation of mid-gap states. Our results are profound for understanding the underlying mechanism of the photocatalytic water oxidation process occurring on $Ag_3PO_4$ surfaces, and serve as a foundation for developing new high-performance $Ag_3PO_4$ based photocatalysts for water splitting and organic contaminant decomposition.

Received 9th March 2017
Accepted 26th April 2017

DOI: 10.1039/c7ra02853a

rsc.li/rsc-advances

Open Access Article. Published on 03 May 2017. Downloaded on 12/10/2025 1:36:53 AM.
This article is licensed under a Creative Commons Attribution-NonCommercial 3.0 Unported Licence.

## 1 Introduction

Direct splitting of water using an efficient photocatalyst is a clean and sustainable technique to produce renewable fuels and has fascinated researchers for over 40 years.[1–3] There has been remarkable progress in developing inorganic and organic systems with high photocatalytic activities for water splitting into $H_2$ and $O_2$ under ultraviolet and visible light, such as n-type $TiO_2$,[4] $NaTaO_3$,[5] $La_2Ti_2O_7$ (ref. 6) and $Sr_2NbO_7$,[7] GaN–ZnO solid solutions,[8,9] and Pt–PdS/CdS[10] *etc.* However, these reported photocatalysts for overall water splitting still suffer from very low quantum efficiency in the visible range, with solar-to-hydrogen efficiencies of less than 0.1%.[11–14] A main reason is that water oxidation to $O_2$ is difficult. The water splitting reaction can be treated in terms of two coupled half-reactions, the $H_2$ evolution reaction (HER) and $O_2$ evolution reaction (OER). The OER is recognized as a much more complicated process and with a much lower reaction rate since the formation of molecular oxygen involves four-electron transfer and occurs on a timescale of *ca.* 5 orders of magnitude slower than $H_2$ evolution.[15–18] This suggests that a hole would easily recombine with an electron before completion of the OER.

In 2010, Yi *et al.* reported a new use of cubic $Ag_3PO_4$ semiconductor, which shows extremely high quantum yield (up to 80–90%) of $O_2$ generation from water oxidation at wavelengths less than 480 nm.[17] They demonstrated that $Ag_3PO_4$ outperforms $BiVO_4$ and $WO_3$ (two of the most well-studied visible-driven water oxidation photocatalysts) in terms of OER rate and dye degradation.[17,19] The origin of its high performance was proposed to be the formation of highly dispersive Ag s–Ag s hybrid bands at the conduction band minimum (CBM), which is advantage for the transfer of carrier to surface.[20] Afterwards, Martin and Bi *et al.* further improved the activity of the $Ag_3PO_4$ by controlling the percentage of exposed facets on crystal surfaces.[15,21] They found that tetrahedral crystals, composed of (111) facets, show a 10 times higher initial oxygen evolution rate than either (110) or (100) facets.[15] Theoretical calculations of the surface energies for these facets have been performed to explain the facet effect on their photocatalytic activity difference.[15,21] However, the value of surface energy is a very limited criterion to assess photocatalytic activity. $Ag_3PO_4$ nanocrystals with

[a]State Key Laboratory of Structural Chemistry, Fujian Institute of Research on the Structure of Matter, Chinese Academy of Sciences, Fuzhou 350002, China. E-mail: wkc@fjirsm.ac.cn

[b]State Key Laboratory of Photocatalysis on Energy and Environment, College of Chemistry, Fuzhou University, Fuzhou 350002, China

† Electronic supplementary information (ESI) available. See DOI: 10.1039/c7ra02853a



This journal is © The Royal Society of Chemistry 2017

Open Access Article. Published on 03 May 2017. Downloaded on 12/10/2025 1:36:53 AM.
This article is licensed under a Creative Commons Attribution-NonCommercial 3.0 Unported Licence.

controlled particle size have been found to exhibit high visible light activity due to the increased specific surface area.[22] Many $Ag_3PO_4$ based composite photocatalysts including $TiO_2$/$Ag_3PO_4$,[23] graphene/$Ag_3PO_4$ (ref. 24 and 25) and Ag/$Ag_3PO_4$ (ref. 26–28) have been prepared to improve photocatalytic activity of $Ag_3PO_4$ by enhancing separation of photogenerated electron–hole pairs. The efficiency of OER on a semiconductor surface is usually determined by four fundamental processes: (i) light absorption; (ii) separation of photoexcited electron–hole pairs; (iii) migration of electrons and holes towards the surface; and (iv) eventual reduction/oxidation reactions.[19] The first three processes take place in the bulk region of the photocatalyst, which have been well studied by the screened hybrid functionals and GW perturbation theory. Nevertheless, the last process, *i.e.* the oxidation/reduction reaction, on $Ag_3PO_4$ surfaces are not at present clear, especially the mechanism of OER. A complete atomic-scale understanding of the OER process on this advancing high efficient visible light photocatalyst is imperative. In this work, particular attentions are focused on the following questions: (i) does the OER take place on $Ag_3PO_4$ (100), (110) and (111) surfaces following the same mechanism as that in a few most reported metal oxides such as $TiO_2$, and nitrides like GaN, and g-$C_3N_4$?[16,18,29–36] If yes, do they have the same rate-limiting step? (ii) What factors lead to the surface-dependent photocatalytic activity of $Ag_3PO_4$ (100), (110) and (111) surfaces? (iii) What role does the surface microstructure have in determining the surface electronic structure and the barrier of OER step?

In the work, we reported a systematic study of the bulk, surface properties and the mechanism of OER on three primary low index facets of $Ag_3PO_4$: (100), (110) and (111) by combining hybrid DFT calculations and first principles thermodynamics. In Section 2, the computational methods and the surface models are presented. The method to calculate the free energy differences between the different reaction steps is briefly introduced. All possible surface terminations for each surface orientation ([100], [110] and [111]) were optimized. In Section 3, we first investigate the bulk properties of $Ag_3PO_4$. They are found to be well reproduced by PBE0 hybrid functional, including accurate band gap and highly dispersive CBM. We then calculate and compare the geometries, surface formation energies, surface electronic structures, and the reaction mechanism steps of the OER of the $Ag_3PO_4$: (100), (110) and (111) surfaces. The theoretical overpotential for the OER at an applied potential $U$ and a given pH is determined. Possible explanations for the surface-dependent photocatalytic activity of $Ag_3PO_4$ are discussed. Lastly, we investigate another two possible mechanisms of the OER on $Ag_3PO_4$ surfaces. We suggested that this study is crucial for the understanding of the photocatalytic process occurring at $Ag_3PO_4$ surfaces. It also provides useful insights for designing better anode materials in (photo) electrochemical water splitting cells.

# 2 Methods and model

## 2.1 Method

Our calculations on the bulk $Ag_3PO_4$ and three primary low index facets of $Ag_3PO_4$: (100), (110) and (111) were performed using the plane-wave basis Vienna Ab initio Simulation Package (VASP) code.[37–39] The projected augmented wave (PAW)[40] potentials with the valence states 2s and 2p for O, 3s and 3p for P, and 4d and 5s for Ag were used to treat the core-valence interaction. The Perdew–Burke–Ernzerhof (PBE) functional[41] was used for the structural optimization. It has been found to reproduce the structural properties of bulk $Ag_3PO_4$.[42] To better describe the exchange–correlation effects of localized electrons, three hybrid functionals (PBE0, HSE03 and HSE06)[43] were used for the electronic structure calculations. The PBE functional was also used for comparison. A $\Gamma$-centered $5 \times 5 \times 5$ Monkhorst–Pack grid for the Brillouin zone sampling[44] and a cutoff energy of 450 eV for the plane wave expansion were found to obtain accurate lattice parameters of the bulk $Ag_3PO_4$.

## 2.2 Model

The (100), (110) and (111) surfaces of $Ag_3PO_4$ were modeled using a period slab with a vacuum space of 15 Å in the direction of surface normal, which is thick enough for the system to converge to an accurate total energy. The atoms in the slab were allowed to fully relax until the residual forces acting on all the constituent ions dropped below 0.05 eV $Å^{-1}$. A $\Gamma$-centered $5 \times 5 \times 1$ Monkhorst–Pack $k$-point grid and a cutoff energy of 450 eV were found to get convergent total and adsorption energies. A self-consistent dipole correction was applied in the direction of surface normal in the structural relaxations and total energy calculations.

The adsorption energy for adsorbate species A was calculated as the energy difference: $\Delta E_{ads} = E_{*A} - (E_* + E_A)$. Where * is the bare surface, *A indicates the adsorption of species A on the surface *, and $E_A$ is the energy of A in its gas state.

## 2.3 Thermodynamics and photocatalysis for OER

The water oxidation reaction can be written as

$$H_2O \rightarrow \tfrac{1}{2}O_2 + 2H^+ + 2e^- \quad (1)$$

We modeled this reaction using the method developed by Norskov and coworkers,[45,46] who have studied the water oxidation on different metal oxide surfaces, such as $TiO_2$, $RuO_2$, and $IrO_2$. The reaction is decomposed into four one-electron steps A–D:

A

$$H_2O + * \rightarrow HO* + H^+ + e^- \quad (2)$$

B

$$HO* \rightarrow O* + H^+ + e^- \quad (3)$$

C

$$H_2O + O* \rightarrow HOO* + H^+ + e^- \quad (4)$$

D

$$HOO* \rightarrow O_2 + * + H^+ + e^- \quad (5)$$

Open Access Article. Published on 03 May 2017. Downloaded on 12/10/2025 1:36:53 AM. This article is licensed under a Creative Commons Attribution-NonCommercial 3.0 Unported Licence.

The above mechanism is the most common one of the water splitting on semiconductor surfaces. We denote this mechanism as mechanism I. It involves the dehydrogenation of $H_2O$, followed by the dissociation of HO* to O*. Subsequently, O* reacts with another $H_2O$ to generate HOO* which then dehydrogenates to $O_2$.[29,45] Another two possible mechanisms (mechanism II involving the HOOH*, mechanism III involving the interaction between O* and HO*) are discussed in Section 3.3.

The method we used in the work concentrates on the thermochemistry of the reaction. We assume that the reaction proceeds through one-electron transfer steps which depend directly on the applied potential. The overpotential needed for the different elementary steps is restricted to the barriers that come from differences of free energies ($\Delta G$) of the intermediates. Kinetic barriers arising from the diffusion of species is not included in the model. From the results, we can evaluate whether OER may take place thermodynamically at a given pH and an applied potential. The details of the calculation of $\Delta G$ are summarized as follows.[45]

Free energy change $\Delta G_0 = \Delta E + \Delta\mathrm{ZPE} - T\Delta S$, with $\Delta E$ denoting the total self-consistent energy change (reaction energy) derived from DFT calculations, $\Delta$ZPE indicating the differences in zero-point energies, and $\Delta S$ indicating the change of entropy. ZPE for the OER intermediates were obtained from the vibrational frequencies. We assume that $S = 0$ for the intermediates adsorbed on the surface, because of the absence of translational and rotational motions upon adsorption. For free gas-phase molecules, we obtained ZPE and $S$ from thermodynamics database.[45]

At standard conditions ($U = 0$, pH $= 0$, $p = 1$ bar, $T = 298$ K), the free energy change of the reaction *AH $\rightarrow$ $H^+ + A + e^-$ is equivalent to that of the reaction *AH $\rightarrow \frac{1}{2}H_2 + A$. Thus, the free energy of $H^+ + e^-$ has been replaced by $\frac{1}{2}H_2$. Under the influence of a potential bias $U$ and an infinite pH, the free energy difference was shifted by $\Delta G(U, \mathrm{pH}) = \Delta G_U + \Delta G_{\mathrm{pH}} = -eU - kT \ln 10 \times \mathrm{pH}$.

In comparison with $H_2O$ and $H_2$, $O_2$ has a much more complicated electronic structure which cannot be described accurately by DFT. In this work, the free energy change of the total reaction $H_2O \rightarrow \frac{1}{2}O_2 + H_2$ is fixed at the experimentally found value of 2.46 eV to avoid the direct calculation of $O_2$ molecule. Hence, the free energy of an $O_2$ molecular can be written as: $G[O_2] = 4.92 - 2E[H_2] + 2E[H_2O] - (\Delta\mathrm{ZPE} - T\Delta S)[2H_2O \rightarrow O_2 + 2H_2]$. More details about this method can be found in the reference by Norskov and coworkers.[45]

Based on above assumptions, the reaction free energy changes ($\Delta G$) for the proposed reaction steps in mechanism I are calculated by the following equations:

$$\Delta G_{\mathrm{A}} = \Delta E_{\mathrm{A}} + 1/2E_{\mathrm{H_2}} - E_{\mathrm{H_2O}} + (\Delta\mathrm{ZPE} - T\Delta S)_{\mathrm{A}} - eU - kT \ln 10 \times \mathrm{pH} \quad (6)$$

$$\Delta G_{\mathrm{B}} = \Delta E_{\mathrm{B}} + 1/2E_{\mathrm{H_2}} + (\Delta\mathrm{ZPE} - T\Delta S)_{\mathrm{B}} - eU - kT \ln 10 \times \mathrm{pH} \quad (7)$$

$$\Delta G_{\mathrm{C}} = \Delta E_{\mathrm{C}} + 1/2E_{\mathrm{H_2}} - E_{\mathrm{H_2O}} + (\Delta\mathrm{ZPE} - T\Delta S)_{\mathrm{C}} - eU - kT \ln 10 \times \mathrm{pH} \quad (8)$$

$$\Delta G_{\mathrm{D}} = 4.92\ \mathrm{eV} + \Delta E_{\mathrm{D}} - 3/2E_{\mathrm{H_2}} + 2E_{\mathrm{H_2O}} + (\Delta\mathrm{ZPE} - T\Delta S)_{\mathrm{D}} - eU - kT \ln 10 \times \mathrm{pH} \quad (9)$$

# 3 Results and discussion

## 3.1 Bulk properties

For reference, we first preliminary investigate the geometry and electronic structure of bulk $Ag_3PO_4$, which have been extensively studied.[20,42,47,48] The optimized equilibrium lattice parameter at PBE level with a $\Gamma$-centered $5 \times 5 \times 5$ $k$-point mesh is 6.087 Å, which is well within the theoretical uncertainties (1.36%) as compared with the experimentally reported values. As illustrated in Fig. 1(a), cubic $Ag_3PO_4$ has $P\bar{4}3n$ symmetry with each atom tetrahedrally coordinated.[17] The $[PO_4]^{3-}$ tetrahedral unit with strong P–O bonds weakens the covalent nature of Ag–O bonds. Umezawa *et al.* suggested that this special structural character inhibits the hybridization of 4d orbitals of Ag and 2p orbitals of O, and forming highly dispersive Ag s–Ag s hybrid bands at CBM. The delocalized charge distribution at CBM results in a small mass of the photoexcited electron, which is advantageous for the transfer of carrier to surface.[20]

It has been proven that the conventional exchange–correlation (XC) functionals such as GGA/PBE and LDA usually underestimate the band gap of semiconductors due to the self-interaction error in the approximate exchange functional.[49,50] Previous studies have confirmed that the band gap of bulk $Ag_3PO_4$ calculated by the LDA and GGA are far smaller than the experimental value.[20,47,48] A hybrid functional that includes a portion of exact exchange can correct much of this error. In this work, three hybrid functionals (PBE0, HSE03 and HSE06) and a PBE functional were adopted for the electronic structure calculation of bulk $Ag_3PO_4$. We find the band gap value of 2.46 eV obtained by PBE0 functional is in good agreement with the experimental value of 2.36 eV.[17] It is also consistent with our previous study.[42] By contrast, the obtained band gap values by using the PBE, HSE03 and HSE06 functionals are 0.18, 1.48, and 1.76 eV, respectively, which all underestimate the band gap. The reason for such a large discrepancy of band gap obtained by different functionals is mainly attributed to the portion of Fock exchange potential included in the calculation of XC energy. The results suggest the importance of using proper XC functional and parameters to obtain an accurate description of electronic structure of $Ag_3PO_4$. The obtained band structure of bulk $Ag_3PO_4$ at PBE0 level is shown in Fig. 1(b). The corresponding total and partial DOS for CB and VB are shown in Fig. 1(c–e). The most desirable characteristic of the electronic structure of bulk $Ag_3PO_4$ is its highly dispersive CBM, which leads to a small effective mass of photoexcited electron. The CBM is mainly composed of the delocalized 5s orbitals of Ag atoms (see Fig. 1(e)). As the formation of the metallic Ag–Ag bond, Ag s –Ag s hybrid orbitals embrace the $[PO_4]^{3-}$ tetrahedral units, which is beneficial for the transfer of photoexcited electrons.[20] The VBM is predominated by O 2p and Ag 4d orbitals, as shown in Fig. 1(d). The relatively flat energy bands near the VBM result in a large effective mass of photoexcited hole. In our previous work, we have determined the effective mass of the

 This journal is © The Royal Society of Chemistry 2017

Open Access Article. Published on 03 May 2017. Downloaded on 12/10/2025 1:36:53 AM.
This article is licensed under a Creative Commons Attribution-NonCommercial 3.0 Unported Licence.

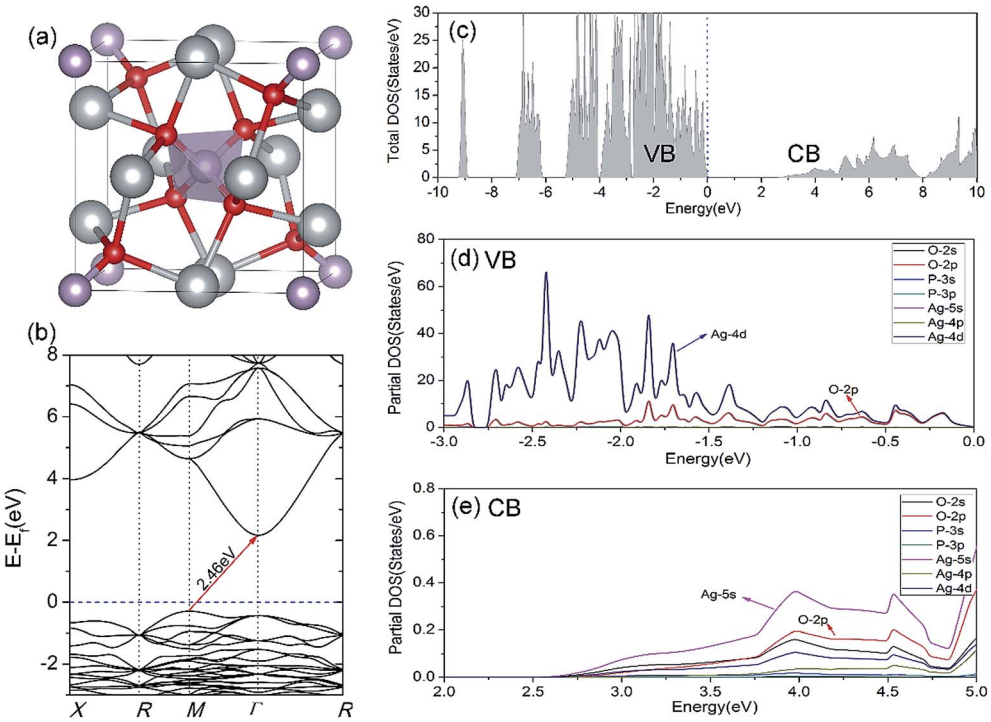


Fig. 1 (a) Crystal structure representation of bulk $Ag_3PO_4$ with indication of $PO_4$ tetrahedral unit in purple. Ag, O, and P atoms are represented by silver, red and purple balls, respectively. (b) Band structure of bulk $Ag_3PO_4$ calculated by the PBE0 functional. The Fermi level was set to the zero of energy. (c) Total DOS of bulk $Ag_3PO_4$. (d) The enlarged plots of the partial DOS of bulk $Ag_3PO_4$ close to the VBM. (e) The enlarged plots of the partial DOS of bulk $Ag_3PO_4$ close to the CBM.

electron $(m_e^*)$ and the hole $(m_h^*)$ of bulk $Ag_3PO_4$ to be $0.47m_e$ and $2.13m_e$, respectively.[42] The value of $m_h^*/m_e^*$ of bulk $Ag_3PO_4$ is 4.5, which is much larger than that of some other ternary oxides photocatalysts such as $BiVO_4$ $(m_h^*/m_e^* \approx 1)$.[50] A significantly different mobility between photoexcited electron and hole results in a low recombination rate of electron–hole pairs. The results suggest that $Ag_3PO_4$ has an excellent band edge for carrier separation. These special inherent characters of bulk $Ag_3PO_4$ actually contributes to a high photocatalytic activity of $Ag_3PO_4$. As the water oxidation process takes place on the surface of photocatalyst, the photocatalytic activity is also strongly affected by the surface properties, which is the subject of next section.

### 3.2 Surface properties

**Structures.** Next, we studied the (100), (110) and (111) surfaces of $Ag_3PO_4$ employing a slab model with a lateral size of $1 \times 1$ unit cell and a thickness that contains six $Ag_3PO_4$ units, as illustrated in Fig. 2. The slab thickness is sufficiently large such that the center region exhibits the corresponding bulk-like structure after fully relaxation.

All possible termination structures for each surface orientation ([100], [110] and [111]) were built and fully optimized. The termination structures and the corresponding formation energies were listed in Fig. S1 and Table S1 in the ESI.† The surface termination with the lowest formation energy for each surface orientation was identified and selected for further study. Here, we briefly introduce the structural characters of these three surfaces. Fig. 2(a–c) present a side view of the most stable geometries for the $Ag_3PO_4$ (100), (110) and (111) surfaces, respectively. It can been seen that the atoms in the top few layers of these surfaces undergo strong rearrangement to minimize the surface energy after fully relaxation. Specifically: (i) (100) surface. The outmost Ag atoms are found to move inward by 0.39 Å after relaxation. The O atoms in the second subsurface tend to move outward. Both the near-surface Ag and O atoms are coordinatively unsaturated. The Ag atoms in the outmost surface are coordinated with two O atoms, while the O atoms are threefold coordinated with two Ag atoms and one P

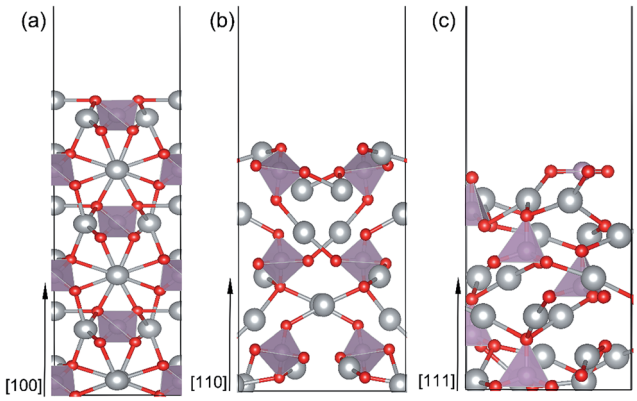


Fig. 2 Side view of the optimized $Ag_3PO_4$ (100) (a), (110) (b) and (111) (c) surfaces.

Open Access Article. Published on 03 May 2017. Downloaded on 12/10/2025 1:36:53 AM.
This article is licensed under a Creative Commons Attribution-NonCommercial 3.0 Unported Licence.

atom. Both Ag and O atoms are fourfold coordinated in the bulk region of $Ag_3PO_4$. The tetrahedral structure of the near-surface $[PO_4]^{3-}$ unit is not distorted much after surface relaxation, indicating the strong P–O covalent bonds in the (100) surface. (ii) (110) surface. Like (100) surface, the outmost under-coordinated Ag and O atoms in (110) surface tend to lie on a plane. The near-surface O atoms are twofold coordinated, and Ag atoms are threefold coordinated. (iii) (111) surface. In the (111) surface, the P and O atoms are displaced on the outmost layer. This is different from the (100) and (110) surfaces, in which the P atoms are not exposed on the outmost surface. The P atom on the top layer of (111) surface coordinates with three O atoms, forming a triangle with P atom at the center. In addition, one single O–P bond with length of 1.49 Å is found on the second subsurface.

**Surface formation energy.** Large surface formation energy has been used as one simple indication for the high photocatalytic activity from theoretical consideration.[15,21,51] With the optimized structures, we calculated the surface formation energy by $E_f = (E_{slab} - E_{bulk})/2A$, where $E_{slab}$ and $E_{bulk}$ are the total energies of the relaxed slab and bulk structures, respectively, $A$ is the surface area, and the factor of 2 indicates the two separate surfaces of the slab model. The number of atoms is the same in calculating the $E_{slab}$ and $E_{bulk}$.

The predicted $E_f$ values for the (100), (110) and (111) surfaces of $Ag_3PO_4$ are 0.34 J m$^{-2}$, 0.38 J m$^{-2}$ and 0.66 J m$^{-2}$, respectively. The obtained relative stability of these three surfaces is consistent with the experimental fact that (111) surface is more reactive than (110) and (100) surfaces.[15] The results also agree with earlier theoretical data of Martin[15] and Bi[21] *et al.* Since the (100) and (110) surfaces have similar atomic arrangement in the outmost surface (containing unsaturated Ag and O atoms), the $E_f$ of (100) surface is thus only a little smaller than that of (110) surface. By contrast, the (111) surface has a significantly larger $E_f$ than that of (110) and (100) surfaces. Such a discrepancy might be ascribed to the presence of more abundant active sites on the (111) surface as compared to the (110) and (100) surfaces.

**Surface electronic structure.** Next, we further examine the electronic structure of the $Ag_3PO_4$ (100), (110) and (111) surfaces at PBE0 level. Fig. 3(a–c) show the total DOS for these three surfaces. We see the total DOS are sensitive to the surface atomic arrangement. For the (100) and (110) surfaces, the highly localized states are formed deep in the gap. In this case, the transition energy of the photon can be reduced, enabling absorption of more solar light. Nevertheless, these mid-gap states may also act as charge carrier recombination centers and reduce the photocatalytic efficiency.[52,53] By contrast, we notice there is no impurity states in the mid-gap of the (111) surface. This can largely avoid the formation of charge carrier recombination centers and improve the photocatalytic efficiency.[52] The origin of the mid-gap states in the (100) and (110) surfaces was further examined by plotting the partial (band decomposed) charge density, as shown in the inset of Fig. 3(a and b). We see the main contributions to the mid-gap states are from the Ag and O atoms in the top three layers of surfaces. The partial DOS analysis (Fig. S3–S5, ESI†) suggests that these mid-gap states are mainly composed of 5s and 4d orbitals of Ag

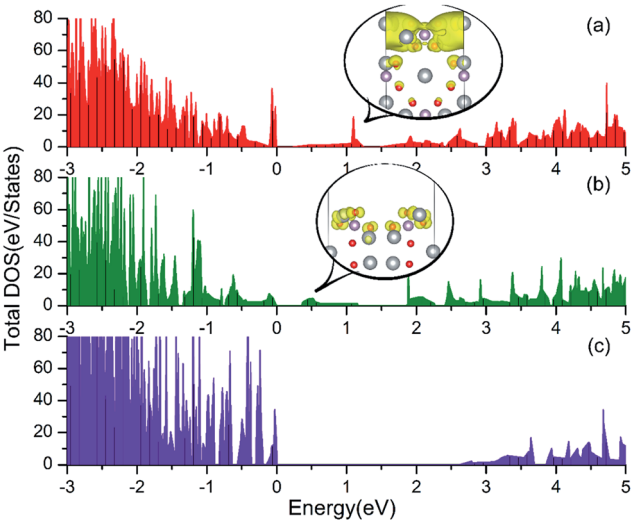


Fig. 3 Total DOS of the $Ag_3PO_4$ (100) (a), (110) (b) and (111) (c) surfaces. The band decomposed charge density for the mid-gap states in the (100) and (110) surfaces are depicted in the inset of (a) and (b), respectively. Here, the color code for the different atoms is as in Fig. 1. The isosurface (yellow surface) is at 0.002 e bohr$^{-3}$ and 0.001 e bohr$^{-3}$ for (100) and (110) surfaces, respectively.

atoms and 2p orbitals of O atoms. From the partial charge density plots, we see that the surface effect extents only a few layers deep. We have further studied the partial DOS of the outmost P and O atoms on the (111) surface. As shown in Fig. S6 (ESI†), we found their PDOS are all located inside the valence band and conduction band. The results suggest that the P atom in the $[PO_3]$ unit on the outmost layer of (111) surface has been satisfied with three P–O bonds. The reorganization of atoms and electrons reduces the unpaired bonds, and therefore prevents mid-gap states in the (111) surface.

### 3.3 Mechanisms of OER

**Adsorption.** Since the free energy curves are quite sensitive to the adsorption energies, as many as possible of the adsorption sites for each adsorbate (HO*, O* and HOO*) were carefully tested. In ESI,† we depicted the initial adsorption sites for each adsorbate on the $Ag_3PO_4$ (100), (110) and (111) surfaces in Fig. S2.† The bottom one-third of the slab was fixed during the relaxation. In total, more than 190 adsorption configurations were optimized. The side views of the most stable adsorption geometries for each adsorbate were displayed in Fig. 4(a–i). The corresponding adsorption energies were listed in Table 1.

*HO*.* As shown in Fig. 4(a), the HO* species is found to be covalently bond to three Ag atoms with the O–H bond perpendicular to the (100) surface plane. Similarly, the most stable adsorption site of HO* on the (110) surface is bond to two Ag atoms (Fig. 4(d)). Specially, the HO* species on the (110) surface also connects with a neighboring O atom *via* a hydrogen bond. The calculated length of the hydrogen bond is 2.02 Å. In contrast, the HO* species on the (111) surface is stabilized by the unsaturated P atom with strong P–O covalent bonding (see Fig. 4(g)). The adsorption energies of the HO* species on the

 This journal is © The Royal Society of Chemistry 2017

Open Access Article. Published on 03 May 2017. Downloaded on 12/10/2025 1:36:53 AM.
This article is licensed under a Creative Commons Attribution-NonCommercial 3.0 Unported Licence.

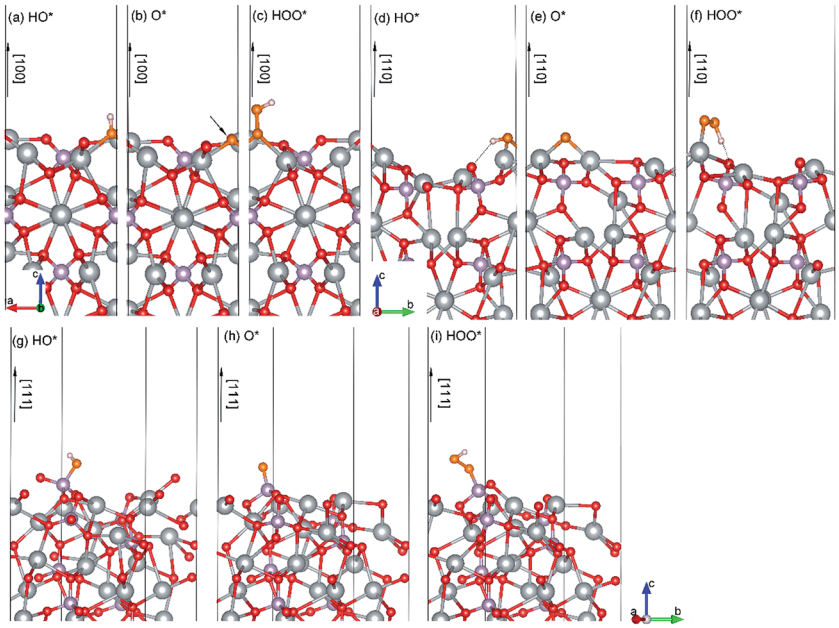


Fig. 4 Side views of the optimized geometries of relevant species (HO*, O*, and HOO*) during OER on $Ag_3PO_4$ (100) (a–c), (110) (d–f) and (111) (g–i) surfaces. The hydrogen bond is indicated by dashed line. The O atoms in the HO*, O*, and HOO* species are indicated as orange spheres.

Table 1 Calculated adsorption energies of HO*, O* and HOO* on $Ag_3PO_4$ (100), (110) and (111) surfaces

| Adsorption energy (eV) | (100) | (110) | (111) |
|---|---|---|---|
| HO | −2.40 | −2.04 | −3.93 |
| O | −2.98 | −2.23 | −4.29 |
| HOO | −1.01 | −1.09 | −2.20 |

(100), (110) and (111) surfaces of $Ag_3PO_4$ are calculated to be −2.40, −2.04, and −3.93 eV, respectively. The much lower value of the adsorption energy for the HO* adsorbed (111) surface is attributed to the formation of strong P–O covalent bonds.

*O**. The O* species is found to be covalently bond to three (two) unsaturated Ag atoms for (100) ((110)) surface, forming an Ag-oxide group. The average Ag–O* bond length of the Ag-oxide group is 2.14 Å for the (100) surface and 2.02 Å for the (110) surface, respectively. The most stable adsorption site of O* on (111) surface is still the on-top site above the unsaturated P atom (Fig. 4(h)). The P–O* bond length is 1.5 Å, which is smaller than that (1.61 Å) in HO* adsorbed (111) surface. It suggests that the dehydrogenation of hydroxyl makes P–O* covalent bond stronger in the (111) surface. The adsorption energy of O* on the (111) surface is found to be −4.29 eV, also significantly lower than that on the (110) and (100) surfaces (−2.23 eV and −2.98 eV, respectively).

*HOO**. The O* species reacts with another $H_2O$ molecular and generates an HOO*. The HOO* species on the (100) surface is also found to be covalently bond to three Ag atoms, but with longer Ag–O average bond length of 2.33 Å as compared to the O* adsorbed (100) surface. The adsorption energy (−1.01 eV) is thus significantly larger than that (−2.98 eV) of O* absorbed (100) surface. The HOO* species on the (110) surface is only bound to one Ag atom with Ag–O bond length of 2.18 Å (Fig. 4(f)). Nevertheless, it is also stabilized by a hydrogen bond with H–O (surface) length of 1.34 Å. The adsorption energy for HOO* absorbed (110) surface is calculated to be −1.09 eV, close to that of HOO* absorbed (100) surface. In the (111) surface, a covalent bond between HOO* and P atom with a P–O bond length of 1.65 Å is formed. It still has the largest adsorption energy (−2.20 eV) as compared to that of HOO* absorbed (100) and (110) surfaces.

**Mechanisms.** The calculated free energy changes for the (100), (110) and (111) facets of $Ag_3PO_4$ following mechanism I (see Fig. 5(a)) at the potential of $U = 0$ and pH = 0 were plotted in Fig. 5(b). From Fig. 5(b), we see that all four steps are uphill for (100) and (110) surfaces. It suggests that each step (A–D) of the OER on (100) and (110) surfaces is endothermic at $U = 0$ and pH = 0. Interestingly, the $\Delta G_A$ was found to be negative (exothermic) for the (111) surface. It indicates that the first deprotonation of the absorbed water molecular becomes to be a favorable step on the (111) surface, compared with the (100) and (110) surfaces. This is attributed to the much lower adsorption energy of HO* on the (111) surface, as illustrated in Table 1. Although there is a significant difference in $\Delta G_A$ between different surfaces, the rate-limiting step for all three surfaces is the step B, *i.e.* the dehydrogenation of HO* (HO* → O* + $H^+$ + $e^-$). This is different with previous studies on other oxides and nitrides surfaces, such as $TiO_2$ (ref. 46) and g-$C_3N_4$,[29,54] in which the rate-limiting step is the step A, that is, the removal of proton from water ($H_2O$ + * → HO* + $H^+$ + $e^-$). The difference in the rate-limiting step is due to the variation of the adsorption strength of HO* among different surfaces. The adsorption energies of HO* on the (100), (110) and (111) facets

Open Access Article. Published on 03 May 2017. Downloaded on 12/10/2025 1:36:53 AM.
This article is licensed under a Creative Commons Attribution-NonCommercial 3.0 Unported Licence.

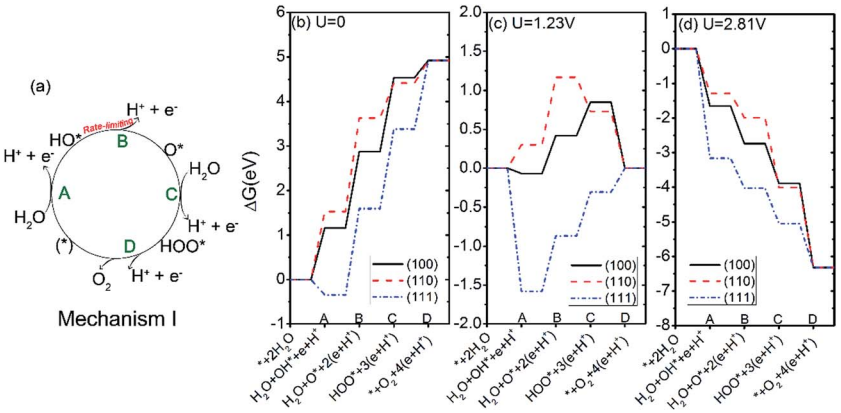


Fig. 5 (a) Oxygen evolution reaction mechanism I; (b–d), the free energies of the intermediates on $Ag_3PO_4$ (100), (110) and (111) surfaces following mechanism I at pH = 0 and $U = 0$ (b), 1.23 V (c), and 2.81 V (d).

of $Ag_3PO_4$ (see Table 1) are significantly lower than that in g-$C_3N_4$ (−1.63 eV)[29] and $TiO_2$ (−1.85 eV).[55] It suggests that the HO species is energetically more favorable to be adsorbed on $Ag_3PO_4$ surfaces than on $TiO_2$ or g-$C_3N_4$ surface. Meanwhile, the dehydrogenation of HO* becomes more difficult on $Ag_3PO_4$ surfaces. At pH = 14, the free energy difference for each step would be decreased by 0.83 eV ($kT$ ln 10 × pH), as illustrated in Fig. S7 in ESI.†

The free energy changes at the equilibrium potential ($U$ = 1.23 V) and pH = 0 were plotted in Fig. 5(c). We see that the steps of A and D of the OER on (100) surface change from uphill to downhill. For the (110) surface, the steps of C and D change from uphill to downhill. For the (111) surface, the $\Delta G$ for the step B, C, and D tend to be less positive compared with $U = 0$. To have every step downhill, an overpotential of 0.49, 0.87, and 0.71 V is required for (100), (110), and (111) surfaces respectively. These values are in the same magnitude as those of other semiconductor oxides like $TiO_2$ (0.78 V),[45] $RuO_2$ (0.37 V)[46] and $IrO_2$ (0.56 V).[46]

Under irradiation, the difference between the $O_2$ evolution redox potential (1.23 V *vs.* NHE) and the redox potential corresponding to the valence band of $Ag_3PO_4$ is assumed to be driving force for the photo-oxidation of water.[29,45] The redox level for the valence band edge $U_{VB}$ of $Ag_3PO_4$ has been found experimentally to be about 2.81 eV for pH = 0.[17] According to Fig. 5(d), the value of $U_{VB}$ provides enough overpotential to compel every step of OER to be downhill for all three surfaces. It suggests that the photoexcited hole in $Ag_3PO_4$ can afford sufficient overpotential for OER to proceed spontaneously on (100), (110), and (111) facets of $Ag_3PO_4$, in good agreement with the experimental findings by Martin and Yi *et al.*[15,17] In particular, the photo-oxidation of water would be more likely to take place on (111) surface than on (110) and (100) surfaces, due to the much lower overpotential for the first step of OER on the (111) surface (−3.16 V) than that on the (100) and (110) surfaces (−1.65 V and −1.28 V, respectively). The results are consistent with previous experimental findings where the tetrahedral $Ag_3PO_4$ crystals, composed of (111) facets, show a higher oxygen evolution rate than either (110) or (100) facets.[15]

We further studied another two possible mechanisms that have been reported in studies of $TiO_2$ and g-$C_3N_4$.[29,45] The two new mechanisms are referred to as mechanism II and III, respectively, as illustrated in Fig. 6(a). In mechanism II, the step A is same as that in mechanism I, *i.e.* the dehydrogenation of $H_2O$. Step B′ is that the absorbed HO* reacts with another water to yield HOOH*. The HOOH* intermediate further dissociates to HOO* in step C′, followed by a dehydrogenation step to $O_2$ in the last step.[29] The four steps of mechanism II can be written as:

A

$$2H_2O + * \rightarrow H_2O + HO^* + H^+ + e^- \quad (10)$$

B′

$$H_2O + HO^* \rightarrow HOOH^* + H^+ + e^- \quad (11)$$

C′

$$HOOH^* \rightarrow HOO^* + H^+ + e^- \quad (12)$$

D

$$HOO^* \rightarrow O_2 + * + H^+ + e^- \quad (13)$$

The mechanism III involves two steps of dehydrogenation of $H_2O$ to produce HO* species (step A and step C″). In step B, one HO* dissociates the hydrogen atom to yield atomic O*. In step D″, the atomic O* eventually reacts with another HO* to generate $O_2$ gas.[29] The four steps of mechanism III can be written as:

A

$$2H_2O + * \rightarrow H_2O + HO^* + H^+ + e^- \quad (14)$$

B

$$H_2O + HO^* \rightarrow H_2O + O^* + H^+ + e^- \quad (15)$$

C″

$$H_2O + O^* \rightarrow HO^* + O^* + H^+ + e^- \quad (16)$$

 This journal is © The Royal Society of Chemistry 2017

Open Access Article. Published on 03 May 2017. Downloaded on 12/10/2025 1:36:53 AM.
This article is licensed under a Creative Commons Attribution-NonCommercial 3.0 Unported Licence.

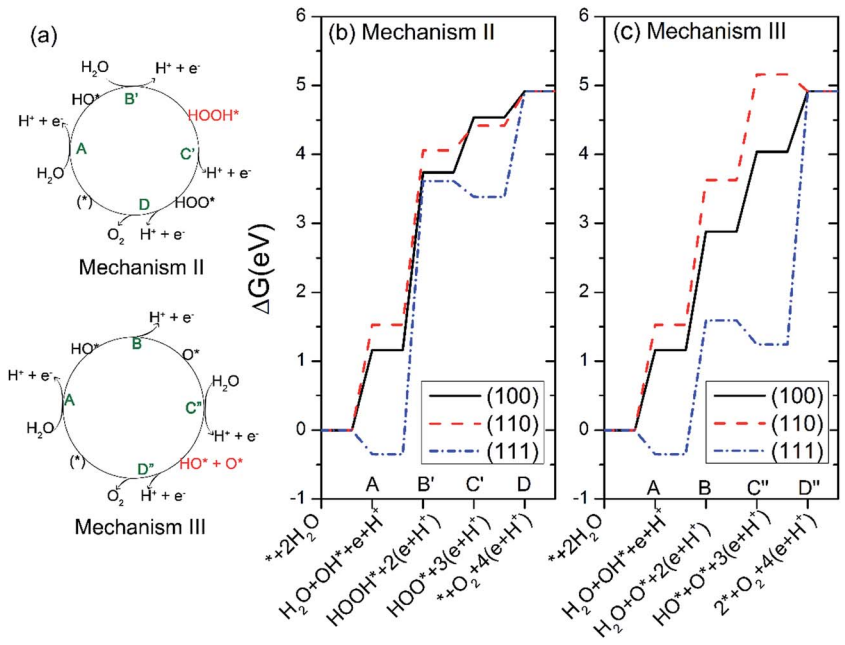


Fig. 6 (a) Oxygen evolution reaction (OER) mechanism II and III. (b and c) The free energies of the intermediates on $Ag_3PO_4$ (100), (110) and (111) surfaces following mechanism II (b) and III (c) at pH = 0 and $U$ = 0.

D″

$$HO^* + O^* \rightarrow O_2 + 2^* + H^+ + e^- \quad (17)$$

The calculated free energies of the intermediates following mechanism II and III at the potential of $U$ = 0 V and pH = 0 were plotted in Fig. 6(b and c), respectively. If the mechanism II is operated, the rate-limiting step for all three surfaces corresponds to the step B′, *i.e.* the formation of HOOH*, as seen from Fig. 6(b). Especially, the free-energy difference of step B′ raises as much as 3.96 eV for the $Ag_3PO_4$ (111) surface at $U$ = 0 and pH = 0. This value has exceeded the valence band edge of $Ag_3PO_4$ ($U_{VB}$ = 2.81 eV), as shown in Fig. 7(a). It indicates that the photoexcited hole in the valence band edge of $Ag_3PO_4$ (111) surface cannot provide sufficient overpotential for the step B′ of mechanism II to proceed. For the (100) and (110) surfaces, the thermodynamic barriers of the rate-limiting step (step B′) following mechanism II are 2.58, and 2.53 eV respectively, which are a little smaller than $U_{VB}$. However, they are much larger than the barriers of rate-limiting step in mechanism I (1.72 eV for (100) surface, 2.1 eV for (110) surface). Therefore, we tend to consider the mechanism II involving a HOOH* intermediate less favorable than mechanism I for the oxidation of water on $Ag_3PO_4$ (100), (110), and (111) surfaces.

In mechanism III, the rate-limiting step for the $Ag_3PO_4$ (100) and (110) surfaces is still the step B (the dehydrogenation of HO*), similar to the mechanism I, as seen from Fig. 6(c). Interestingly, in comparison with mechanism I, the rate-limiting step for the $Ag_3PO_4$ (111) surface changes from step B to step D″, in which O* reacts with an HO* to generate $O_2$ gas. The corresponding barrier of rate-limiting step for (111) surface increases from 1.94 eV to 3.68 eV at $U$ = 0, which also exceeds the maximum potential energy gain from irradiation. Fig. 7(b) shows that step D″ is an endothermic process for $Ag_3PO_4$ (111) surface even under the irradiation ($U$ = 2.81 V). Therefore, we conclude that the mechanism II and III are unlikely to take place on the $Ag_3PO_4$ (111) surface. For (100) surface, the barrier of step C in mechanism I is larger than that of step C″ in mechanism III. Therefore, the OER process would like to proceed by following mechanism III for (100) surface. For (110) surface, the mechanism I is more likely to take place as $\Delta G_C^I < \Delta G_{C''}^{III}$.

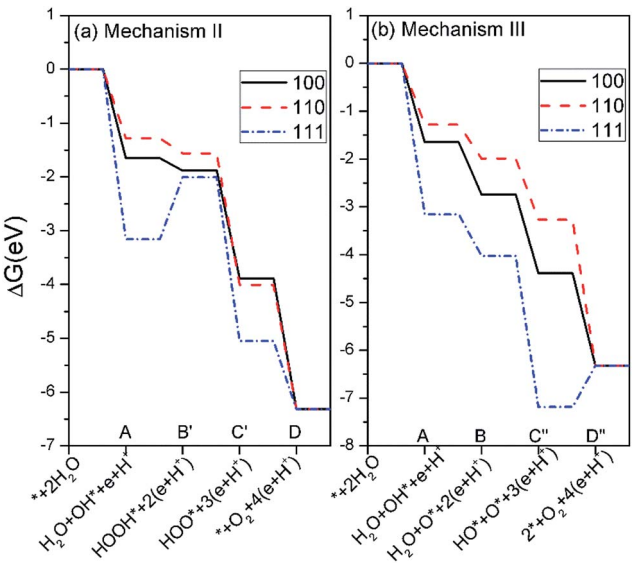


Fig. 7 The free energies of the intermediates on $Ag_3PO_4$ (100), (110) and (111) surfaces following mechanism II (a) and III (b) at pH = 0 and $U$ = 2.81 V.

Open Access Article. Published on 03 May 2017. Downloaded on 12/10/2025 1:36:53 AM.
This article is licensed under a Creative Commons Attribution-NonCommercial 3.0 Unported Licence.

# 4 Conclusions

We report here a comparative study of the bulk, surface properties and the photo-oxidation of water on three low index facets of $Ag_3PO_4$: (100), (110) and (111) based on the first-principles DFT and the thermochemistry of the reaction steps. The conclusions are as follows: (1) for all three surfaces, the rate-limiting step for the OER process is the dehydrogenation of HO* (HO* $\rightarrow$ O* + $H^+ + e^-$); (2) oxidation of water on the $Ag_3PO_4$ (100), (110), and (111) surfaces requires an overpotential of 0.49, 0.87, and 0.71 V respectively at the equilibrium potential ($U$ = 1.23 V) and pH = 0; (3) the first proton removal of water (step A: $H_2O$ + * $\rightarrow$ HO* + $H^+ + e^-$) is sensitive to the crystalline surface structures. At $U = 0$ and pH = 0, the free energy changes of step A ($\Delta G_A$) on (100) and (110) surfaces are endothermic, while $\Delta G_A$ is calculated to be negative (exothermic) for (111) surface. The much lower adsorption energy of HO* on (111) surface leads to the deprotonation of the first absorbed water molecular becoming to be a favorable step in (111) surface, compared with (100) and (110) surfaces; (4) the illumination of the $Ag_3PO_4$ (100), (110), and (111) surfaces with light provides enough overpotential for the photooxidation to proceed spontaneously; (5) the OER process tends to proceed by following mechanism III on the (100) surface. By contrast, the (110) and (111) surfaces would like to oxide water by following mechanism I; (6) the total DOS plots are strongly related to the surface geometry. For the (100) and (110) surfaces, the highly localized states are formed deep in the gap. In contrast, there is no impurity states in the mid-gap of (111) surface. This can largely avoid the formation of charge carrier recombination centers and improve the visible photocatalytic efficiency. Our results are important for understanding the underlying mechanism of the photocatalytic water oxidation process occurring at $Ag_3PO_4$ surfaces, and serve as a foundation for developing new high-performance $Ag_3PO_4$ based photocatalysts for water splitting.

# Acknowledgements

This work was supported by the National Science Foundation of China (No. 21501177, 21673240, and 21201165) and the Special Program for Applied Research on Super Computation of the NSFC-Guangdong Joint Fund (the second phase). The authors also gratefully acknowledge the National Supercomputing Center in Shenzhen for providing the computing resources.

# References

1 X. Chen, S. Shen, L. Guo and S. S. Mao, *Chem. Rev.*, 2010, **110**, 6503–6570.
2 A. Kudo and Y. Miseki, *Chem. Soc. Rev.*, 2009, **38**, 253–278.
3 A. Fujishima and K. Honda, *Nature*, 1972, **238**, 37–38.
4 S. U. M. Khan, M. Al-Shahry and W. B. Ingler, *Science*, 2002, **297**, 2243–2245.
5 H. Kato, K. Asakura and A. Kudo, *J. Am. Chem. Soc.*, 2003, **125**, 3082–3089.
6 H. G. Kim, D. W. Hwang, S. W. Bae, J. H. Jung and J. S. Lee, *Catal. Lett.*, 2003, **91**, 193–198.
7 A. Kudo, H. Kato and S. Nakagawa, *J. Phys. Chem. B*, 2000, **104**, 571–575.
8 K. Maeda, K. Teramura, D. L. Lu, T. Takata, N. Saito, Y. Inoue and K. Domen, *Nature*, 2006, **440**, 295.
9 K. Maeda, T. Takata, M. Hara, N. Saito, Y. Inoue, H. Kobayashi and K. Domen, *J. Am. Chem. Soc.*, 2005, **127**, 8286–8287.
10 H. Yan, J. Yang, G. Ma, G. Wu, X. Zong, Z. Lei, J. Shi and C. Li, *J. Catal.*, 2009, **266**, 165–168.
11 J. Liu, Y. Liu, N. Liu, Y. Han, X. Zhang, H. Huang, Y. Lifshitz, S.-T. Lee, J. Zhong and Z. Kang, *Science*, 2015, **347**, 970–974.
12 V. Balzani, A. Credi and M. Venturi, *ChemSusChem*, 2008, **1**, 26–58.
13 H. B. Gray, *Nat. Chem.*, 2009, **1**, 7.
14 I. Tsuji, H. Kato and A. Kudo, *Angew. Chem., Int. Ed.*, 2005, **44**, 3565–3568.
15 D. J. Martin, N. Umezawa, X. Chen, J. Ye and J. Tang, *Energy Environ. Sci.*, 2013, **6**, 3380–3386.
16 W. N. Zhao and Z. P. Liu, *Chem. Sci.*, 2014, **5**, 2256–2264.
17 Z. G. Yi, J. H. Ye, N. Kikugawa, T. Kako, S. X. Ouyang, H. Stuart-Williams, H. Yang, J. Y. Cao, W. J. Luo, Z. S. Li, Y. Liu and R. L. Withers, *Nat. Mater.*, 2010, **9**, 559–564.
18 Y.-F. Li, Z.-P. Liu, L. Liu and W. Gao, *J. Am. Chem. Soc.*, 2010, **132**, 13008–13015.
19 D. J. Martin, G. G. Liu, S. J. A. Moniz, Y. P. Bi, A. M. Beale, J. H. Ye and J. W. Tang, *Chem. Soc. Rev.*, 2015, **44**, 7808–7828.
20 N. Umezawa, O. Y. Shuxin and J. H. Ye, *Phys. Rev. B: Condens. Matter Mater. Phys.*, 2011, **83**, 035202.
21 Y. Bi, S. Ouyang, N. Umezawa, J. Cao and J. Ye, *J. Am. Chem. Soc.*, 2011, **133**, 6490–6492.
22 D. Cao-Thang, N. Thanh-Dinh, F. Kleitz and D. Trong-On, *Chem. Commun.*, 2011, **47**, 7797–7799.
23 W. Yao, B. Zhang, C. Huang, C. Ma, X. Song and Q. Xu, *J. Mater. Chem.*, 2012, **22**, 4050–4055.
24 Q. Xiang, D. Lang, T. Shen and F. Liu, *Appl. Catal., B*, 2015, **162**, 196–203.
25 X. Yang, H. Cui, Y. Li, J. Qin, R. Zhang and H. Tang, *ACS Catal.*, 2013, **3**, 363–369.
26 Y. Liu, L. Fang, H. Lu, L. Liu, H. Wang and C. Hu, *Catal. Commun.*, 2012, **17**, 200–204.
27 Y. Liu, L. Fang, H. Lu, Y. Li, C. Hu and H. Yu, *Appl. Catal., B*, 2012, **115**, 245–252.
28 Y. Bi, H. Hu, S. Ouyang, Z. Jiao, G. Lu and J. Ye, *J. Mater. Chem.*, 2012, **22**, 14847–14850.
29 S. Lin, X. Ye, X. Gao and J. Huang, *J. Mol. Catal. A: Chem.*, 2015, **406**, 137–144.
30 J. Chen, Y.-F. Li, P. Sit and A. Selloni, *J. Am. Chem. Soc.*, 2013, **135**, 18774–18777.
31 Y. Ji, B. Wang and Y. Luo, *J. Phys. Chem. C*, 2014, **118**, 1027–1034.
32 Y. Ji, B. Wang and Y. Luo, *J. Phys. Chem. C*, 2012, **116**, 7863–7866.
33 A. V. Akimov, J. T. Muckerman and O. V. Prezhdo, *J. Am. Chem. Soc.*, 2013, **135**, 8682–8691.
34 R. Long and O. V. Prezhdo, *J. Am. Chem. Soc.*, 2014, **136**, 4343–4354.

 This journal is © The Royal Society of Chemistry 2017

Open Access Article. Published on 03 May 2017. Downloaded on 12/10/2025 1:36:53 AM.
This article is licensed under a Creative Commons Attribution-NonCommercial 3.0 Unported Licence.

35 W. R. Duncan, W. M. Stier and O. V. Prezhdo, *J. Am. Chem. Soc.*, 2005, **127**, 7941–7951.
36 A. V. Akimov, A. J. Neukirch and O. V. Prezhdo, *Chem. Rev.*, 2013, **113**, 4496–4565.
37 G. Kresse, *Vienna ab initio simulation package (VASP), 5.3.5*, 2014, http://cms.mpi.univie.ac.at/vasp/vasp/vasp.html.
38 G. Kresse and J. Furthmuller, *Phys. Rev. B: Condens. Matter*, 1996, **54**, 11169–11186.
39 G. Kresse and D. Joubert, *Phys. Rev. B: Condens. Matter*, 1999, **59**, 1758–1775.
40 P. E. Blochl, *Phys. Rev. B: Condens. Matter*, 1994, **50**, 17953–17979.
41 J. P. Perdew, K. Burke and M. Ernzerhof, *Phys. Rev. Lett.*, 1996, **77**, 3865–3868.
42 Z. Ma, Z. Yi, J. Sun and K. Wu, *J. Phys. Chem. C*, 2012, **116**, 25074–25080.
43 J. Heyd, G. E. Scuseria and M. Ernzerhof, *J. Chem. Phys.*, 2003, **118**, 8207–8215.
44 H. J. Monkhorst and J. D. Pack, *Phys. Rev. B: Condens. Matter*, 1976, **13**, 5188.
45 A. Valdes, Z. W. Qu, G. J. Kroes, J. Rossmeisl and J. K. Norskov, *J. Phys. Chem. C*, 2008, **112**, 9872–9879.
46 J. Rossmeisl, Z. W. Qu, H. Zhu, G. J. Kroes and J. K. Norskov, *J. Electroanal. Chem.*, 2007, **607**, 83–89.
47 J. J. Liu, X. L. Fu, S. F. Chen and Y. F. Zhu, *Appl. Phys. Lett.*, 2011, **99**, 191903.
48 X. G. Ma, B. Lu, D. Li, R. Shi, C. S. Pan and Y. F. Zhu, *J. Phys. Chem. C*, 2011, **115**, 4680–4687.
49 S. Lany and A. Zunger, *Phys. Rev. B: Condens. Matter Mater. Phys.*, 2008, **78**, 235104.
50 A. Walsh, Y. Yan, M. N. Huda, M. M. Al-Jassim and S.-H. Wei, *Chem. Mater.*, 2009, **21**, 547–551.
51 B. J. Zheng, X. Wang, C. Liu, K. Tan, Z. X. Xie and L. S. Zheng, *J. Mater. Chem. A*, 2013, **1**, 12635–12640.
52 Z. Ma, K. Wu, R. Sa, Q. Li, C. He and Z. Yi, *Int. J. Hydrogen Energy*, 2015, **40**, 980–989.
53 K. Yang, Y. Dai and B. Huang, *J. Phys. Chem. C*, 2007, **111**, 12086–12090.
54 J. Wirth, R. Neumann, M. Antonietti and P. Saalfrank, *Phys. Chem. Chem. Phys.*, 2014, **16**, 15917–15926.
55 A. Hussain, J. Gracia, B. E. Nieuwenhuys and J. W. Niemantsverdriet, *ChemCatChem*, 2013, **5**, 2479–2488.